

1 Structure and anisotropy of the Mexico subduction
2 zone based on Rayleigh-wave analysis and
3 implications for the geometry of the Trans-Mexican
4 Volcanic Belt

I. Stubailo,¹ C. Beghein,¹ P. M. Davis,¹

Corresponding author: I. Stubailo (stubailo@ess.ucla.edu)

¹Department of Earth and Space Sciences,
University of California Los Angeles, CA
90095, USA.

5 **Abstract.** We develop a three-dimensional model of shear-wave veloc-
6 ity and anisotropy for the Mexico subduction zone using Rayleigh wave phase
7 velocity dispersion measurements. This region is characterized by both steep
8 and flat subduction and a volcanic arc that appears to be oblique to the trench.
9 We give a new interpretation of the volcanic arc obliqueness and the loca-
10 tion of the Tzitzio gap in volcanism based on the subduction morphology.

11 We employ the two-station method to measure Rayleigh phase velocity dis-
12 persion curves between periods of 16 s to 171 s. The results are then inverted
13 to obtain azimuthally anisotropic phase velocity maps and to model 3-D vari-
14 ations in upper mantle velocity and anisotropy. Our maps reveal lateral vari-
15 ations in phase velocity at all periods, consistent with the presence of flat
16 and steep subduction. We also find that the data are consistent with two lay-
17 ers of anisotropy beneath Mexico: a crustal layer, with the fast directions par-
18 allel to the North American absolute plate motion, and a deeper layer that
19 includes the mantle lithosphere and the asthenosphere, with the fast direc-
20 tion interpreted in terms of toroidal mantle flow around the slab edges.

21 Our combined azimuthal anisotropy and velocity model enables us to an-
22 alyze the transition from flat to steep subduction and to determine whether
23 the transition involves a tear resulting in a gap between segments or is a con-
24 tinuous deformation caused by a lithospheric flexure. Our anisotropy results
25 favor a tear, which is also consistent with the geometry of the volcanic belt.

1. Introduction

26 The evolution, origin, and structure of the Mexican subduction zone have been studied
27 using a variety of techniques over the years (*Truchan et al.*,1973; *Pardo and Suarez*,1995;
28 *Manea et al.*,2005; *Kanjorski*, 2003). Global plate reconstruction indicates that the Far-
29 allon plate fragmented about 23 Ma ago, at which point two new plates were created: the
30 Cocos plate to the North and the Nazca plate to the South (*Atwater and Stock*, 1998;
31 *Mann et al.*, 2007; *Lonsdale*, 1991). About 13 Ma later, the Rivera plate came into
32 existence by separating from the Cocos plate.

33 Based on seismicity, focal mechanisms, and the slab geometry determined from the
34 hypocenter locations of local events, the area under Mexico can be split into several
35 sections (*Pardo and Suarez*, 1995): (1) the Jalisco section, where the Rivera plate subducts
36 steeply at approximately 50° , (2) the Michoacan section, where the dip of the Cocos plate
37 undergoes a transition from steep to almost parallel to the surface, (3) the Guerrero-
38 Oaxaca section, where the slab is flat for about 250 km, and (4) the southern Oaxaca
39 and Chiapas section, where the dip of the Cocos plate increases up to 30° . As a result
40 of the complex subduction, the Trans-Mexican Volcanic Belt (TMVB), which consists of
41 nearly 8000 volcanoes, is apparently oblique to the Trench instead of being parallel to it
42 (Figure 1).

43 Detailed information on the slab depth under the transect from Acapulco to Tampico has
44 been obtained from the teleseismic data collected during the Middle America Subduction
45 Experiment (MASE) (*Perez-Campos et al.*, 2008; *Husker*, 2008; *Iglesias et al.*, 2010). The
46 results based on receiver function analysis (*Perez-Campos et al.*, 2008) and body wave

47 tomography (*Husker, 2008; Husker and Davis, 2009*) show an approximately 40 km thick,
48 flat, shallow slab, that starts dipping inland 250 km away from the trench at approximately
49 a 74° angle, and that is truncated at 500 km depth. The flat subduction under the MASE
50 array is consistent with the prior study by *Pardo and Suarez (1995)*. A two-dimensional(2-
51 D) slab image based on the S-wave velocity was also obtained by *Iglesias et al. (2010)*
52 using regional earthquakes. The authors described a well-resolved low-velocity zone below
53 the TMVB consistent with the presence of a mantle wedge. *Chen and Clayton (2009)*
54 showed low attenuation associated with the subducting part of the slab (forearc) and
55 high attenuation near the mantle wedge and beneath the TMVB. The authors interpreted
56 the high-attenuation zone in the mantle wedge as related to relatively high temperature,
57 fluids, and partial melts produced during the subduction process. The current 2-D view
58 of the slab under the Central Mexico region (MASE line) based on those prior studies
59 (*Kim et al., 2006; Husker, 2008*) is shown in Figure 2.

60 In this study, we use data from networks with unprecedented dense coverage to develop
61 a 3-D model of S-wave velocity and azimuthal anisotropy of the Mexican subduction zone.
62 The azimuthal anisotropy is the dependence of local seismic propagation characteristics
63 on the azimuth of propagation. The 3-D nature of our results allows for better under-
64 standing of the interaction between the subducting slab, the mantle lithosphere, and the
65 asthenosphere.

66 Seismic anisotropy is important to study since it can provide insights into the defor-
67 mation history of the region. It can arise from the lattice preferred orientation (LPO)
68 of intrinsically anisotropic crystals or from the shape preferred orientation of isotropic
69 materials with contrasting elastic properties (*Karato, 1998*). Anisotropy in the crust may

70 be caused by mineral fabrics, preferentially oriented fluid-filled cracks, and the presence
71 of faults (*Crampin et al.*, 1984). In the upper mantle, it is often attributed to the LPO
72 of olivine over large scales, and therefore can give information on the past and current
73 deformation processes in the lithosphere and asthenosphere, respectively (*Karato*, 1998;
74 *Silver*, 1996).

75 To obtain a 3-D model of the Mexican subduction zone, we perform dispersion measure-
76 ments of Rayleigh waves for periods of 16-171 s and show that Rayleigh phase velocities
77 depend on the azimuth of propagation. The dense network of seismic stations used here
78 and the analysis based on surface waves, which inherently have better depth sensitiv-
79 ity to structure than body waves, allow us to obtain a higher-resolution velocity and
80 anisotropy model than in previous studies. The combined 3-D models of S-wave veloci-
81 ties and anisotropy enable us to infer information about the dynamics of the subduction
82 process in the region.

2. Data

83 We use data collected by several networks on a total of 181 stations (Figure 3): the
84 Mesoamerican Seismic Experiment (MASE, 100 stations), the Network of Autonomously
85 Recording Seismographs (NARS, 15 stations), USArray (24 stations), Mapping the Rivera
86 Subduction Zone (MARS, 9 stations), and the Mexican Servicio Sismologico Nacional
87 (SSN, 33 stations). All the Z-component waveforms used are down-sampled to 1 sample
88 per second and corrected for the instrument response to eliminate phase distortion at
89 higher frequencies.

90 Our data selection is tailored to the two-station method (*Sato*, 1955; *Brune and Dor-*
91 *man*, 1963; *Knopoff et al.*, 1967; *Herrmann*, 1987), which allows us to measure phase

92 velocities between two stations that share a common great-circle path with an event.
93 This method has the advantage over single-station phase velocity measuring techniques of
94 removing uncertainties related to the source and to the path between the source and its
95 near station. The codes employed here are based on the method developed by *Herrmann*
96 (1987) as implemented by J.A. Snoke (*Warren et al.*, 2008). We identify combinations of
97 station pairs and events for which the angles between the great circles are no larger than
98 3° (Figure 4). To have suitable signal-to-noise ratio (SNR), we further restrict ourselves to
99 events with moment magnitude 6.0 and larger in the USGS catalog and depths shallower
100 than 250 km.

101 We perform a frequency-time analysis (FTAN) (*Landisman et al.*, 1969; *Dziewonski et*
102 *al.*, 1969) for each earthquake and station, to assess data quality and to determine the
103 appropriate time and velocity windows to be used to filter the data for further processing.
104 By choosing these windows, we isolate the fundamental mode surface waves from the
105 overtones, a requirement to calculate the Green's function correctly. Events and stations
106 with low signal-to-noise ratio or irregular FTAN plots (Figure 5) are rejected. We also
107 reject pairs of stations for which the phase velocities differ for earthquakes arriving from
108 opposite sides. For instance, if the phase velocity determined for station pair STA1-STA2
109 does not fall within the uncertainties estimated for the phase velocity of station pair
110 STA2-STA1, the measurements for that station pair are rejected. Such phase velocity
111 discrepancies can be caused by paths that cross tectonic boundaries at sharp angles leading
112 to refraction, multipathing, and scattering. Examples of such event locations are Northern
113 Chile, Southern Peru, and Western Canada, which produce arrival paths parallel to the
114 Mexico coast for many sites not far inland.

3. Interstation phase velocity measurements

115 Based on the criteria described in section 2, we are able to identify 7602 station pairs
116 corresponding to 116 teleseismic events recorded between 2005 and 2009. If a pair of
117 stations is linked to multiple events, we average the dispersion curve measurements. After
118 averaging the dispersion curves, we are left with 5050 interstation phase velocity curves
119 (with up to 12 events per path) for the periods of 16, 18, 20, 22, 25, 28, 33, 38, 44, 54,
120 68, 85, 102, 128, and 171 seconds. The path density for the selected events is higher to
121 the west of the study area (Figure 3), but overall the selected paths result in excellent
122 coverage as shown by the resolution tests described in section 4.

123 The interstation method employed uses a reference phase velocity spectrum calculated
124 for a local reference Earth model to remove the need for phase unwrapping. Our local
125 reference Earth model (hereafter referred to as mTNA) is a composite model, modified
126 from the upper mantle shear-wave velocity Tectonic North America (TNA) model (*Grand
127 and Helmberger, 1984*) by adding the P-wave velocities and densities from model AK135
128 (*Kennett et al., 1995*), and the Crust 2.0 crustal model (*Bassin et al., 2000*). This reference
129 model is shown in Figure 6 and described in Table 1. Phase velocity uncertainties are
130 determined based on the coherence of the two waveforms after the near-station waveform
131 has been time-shifted to the far-station epicentral distance using the calculated phase
132 velocities (see details in *Warren et al., 2008*).

133 Examples of interstation measurements made along the MASE array at three different
134 locations with respect to the slab are shown in Figure 7. The interstation phase velocity
135 measurements vary systematically along the MASE array, with a decrease in phase velocity
136 from southwest to northeast, away from the subducting slab. The higher phase velocities

137 are thus located above the region of flat slab subduction, consistent with the tomographic
 138 body-wave inversion of *Husker and Davis (2009)*.

4. Azimuthally anisotropic phase velocity maps

4.1. Method

The two-station technique employed here enables us to measure path-averaged phase velocities \bar{c} between two stations :

$$\bar{c}(T) = \frac{1}{d_2 - d_1} \int_{d_1}^{d_2} c(T, l) dl \quad (1)$$

139 where T indicates the period considered, and stations 1 and 2 are located along the
 140 great-circle path l at epicentral distances d_1 and d_2 , respectively. We invert our path-
 141 averaged phase velocity measurements using the least-squares (LSQR) method developed
 142 by Lebedev (*Darbyshire and Lebedev (2009)*) and previously employed by *Beghein et al.*
 143 (2010). With this method, the study area is parameterized by a 2-D triangular grid. The
 144 choice of the grid spacing is subjective, but the spacing should remain smaller than the
 145 features we are trying to resolve, which themselves is depend on the station spacing and the
 146 azimuthal coverage achieved. Cells that are too large would smooth the data unnecessarily
 147 and potentially hide interesting model features, while cells that are too small could display
 148 variations that are not resolvable with our data. After testing parameterization with 45,
 149 60, and 100 km spacing, we select the grid spacing of 60 km (for the total of 898 grid
 150 cells).

This method not only enables us to obtain isotropic phase velocity maps at different periods, but also allows us to model the azimuthal dependence of the phase velocity. In

a slightly anisotropic medium, phase velocities can be expressed as (*Smith and Dahlen, 1973*):

$$c(T, \Psi) = c_0(T) + c_1(T)\cos(2\Psi) + c_2(T)\sin(2\Psi) + c_3(T)\cos(4\Psi) + c_4(T)\sin(4\Psi) \quad (2)$$

where c is the phase velocity, T is the period, Ψ is the azimuth, $c_0(T)$ is the isotropic term, and c_{1-4} are the azimuthal coefficients (*Backus, 1970*). The directions Θ of fast propagation for Rayleigh waves and the amplitude A of the anisotropy can be obtained using :

$$\Theta_{2\Psi} = 1/2 \arctan(c_2/c_1), \quad (3)$$

$$\Theta_{4\Psi} = 1/4 \arctan(c_4/c_3), \quad (4)$$

$$A_{2\Psi} = \sqrt{(c_1^2 + c_2^2)}, \quad (5)$$

$$A_{4\Psi} = \sqrt{(c_3^2 + c_4^2)}. \quad (6)$$

151 Like most geophysical inverse problems, the inversion of Eq. 1 is non-unique, which
 152 means that a subjective regularization has to be imposed. The anisotropic and isotropic
 153 terms are smoothed independently, and each period is treated separately from the others.
 154 We use the trade-off curves (or L-curves) to choose a damping value for each period (Figure
 155 8). The preferred damping is chosen near the corner of the L-curve. After a damping value
 156 is chosen for the isotropic term, we proceed with varying the damping for the anisotropic
 157 terms (first the 2Ψ terms, then the 4Ψ terms, independently). Even though dispersion
 158 curves are obtained for periods between 16 s and 171 s, our ray coverage is not sufficient to

159 reasonably resolve phase velocity anomalies at periods greater than 100 s (a large damping
 160 is needed and no significant variation in phase velocity is found). We thus focus the rest
 161 of the manuscript on the results obtained at periods between 16 s and 100 s.

162 To evaluate the significance of the reduction in misfit χ^2 when adding anisotropy, we
 163 perform standard F-tests (*Bevington and Robinson, 1992*) following the method described
 164 by *Trampert and Woodhouse (2003)*: we vary the damping and compute the χ^2 misfit and
 165 the trace of the resolution matrix \mathbf{R} for the isotropic model, for the $0\Psi+2\Psi$ model, and
 166 for the model that includes all anisotropic terms (0Ψ , 2Ψ , and 4Ψ).

The resolution matrix \mathbf{R} , which is not readily calculated by the LSQR method, is determined for various damping values following *Trampert and Woodhouse (2003)*. Each column j of the matrix \mathbf{G} that describes the physical relation between the data and the model parameters is inverted:

$$R_j = \mathbf{L}G_j \quad (7)$$

167 where R_j is column j of matrix \mathbf{R} , \mathbf{L} is the LSQR operator, and G_j is column j of matrix
 168 \mathbf{G} . In our case, \mathbf{R} is a 4490x4490 matrix, with 898 rows and columns for the isotropic part,
 169 1796 rows and columns containing 2Ψ sin and cos components, and 1796 rows and columns
 170 with 4Ψ sin and cos components (see Eq. 2). Figure 9 displays χ^2 as a function of the
 171 trace of \mathbf{R} for the isotropic and anisotropic inversions for the period of 28 s. This Figure,
 172 combined with the F-tests, shows that the 2Ψ terms are needed to explain the data, but
 173 the 4Ψ terms do not improve the data fit significantly. We obtain similar outcomes for the
 174 other periods. Hence, in the following, we discuss only the isotropic (0Ψ) and 2Ψ terms.

175 To evaluate the quality of our data coverage, we conduct isotropic and anisotropic
 176 resolution tests for all periods. Figures 10 and 11 show three representative tests at a
 177 period of 44 s: (1) a test of the isotropic inversion with a checkerboard input (Figure 10),
 178 (2) a test of the anisotropic inversion with a purely isotropic input (Figure 11, A and
 179 B), and (3) a test of the anisotropic inversion with an isotropic input and anisotropy
 180 (Figure 11, C and D). In the anisotropic tests, the isotropic inputs are chosen to coincide
 181 with our preferred phase velocity model at the period considered. Figures 10 and 11
 182 demonstrate that the input isotropic and anisotropic models are well recovered in the
 183 middle of the study area, close to the MASE array, marked by the green line on the figures,
 184 with some discrepancies and smearing north of 21° latitude and east of 96° longitude
 185 (shaded area in the figures). We find that an anisotropic inversion of an isotropic input
 186 model (Figure 11A and B) yields an output model with virtually no anisotropy (less than
 187 0.5%) everywhere in the study area. Because the resolution of our models is better in
 188 the center of our study area, where the number of stations, and therefore the number of
 189 crossing paths, is higher, we will concentrate the discussion of the results on that part of
 190 the region.

191 Trade-offs between isotropic and anisotropic terms in the inversion of Eq. 1 can affect
 192 the results. The synthetic tests shown in Fig. 11A and B demonstrate that our inversion
 193 scheme can detect the absence of anisotropy, and therefore that there is little trade-off
 194 between the isotropic and anisotropic terms. Another way to analyze these trade-offs is
 195 by computing the resolution matrix \mathbf{R} from Eq. 7, which we do using the damping values
 196 chosen for our preferred anisotropic model (Figure 12). Each line of \mathbf{R} corresponds to
 197 a model parameter, and the matrix is divided into nine sub-matrices $c_i c_j$ ($i, j = 0, 1, 2$),

198 where c_0 spans parameters that correspond to the 0Ψ term, and c_1 and c_2 span parameters
199 that correspond to the two 2Ψ terms. The off-diagonal submatrices $c_i c_j$ ($i \neq j$), represent
200 trade-offs between the three terms, and the off-diagonal elements within the submatrices
201 $c_i c_i$ indicate lateral trade-offs, i.e. trade-off within the same c_i term but at different
202 geographic locations. Figure 12 shows the existence of some lateral trade-offs, which result
203 from imperfect ray coverage and lateral smoothing. It also demonstrates that trade-offs
204 exist between the isotropic and anisotropic terms and between the two 2Ψ terms, but
205 that they are relatively small. The synthetic tests performed in addition to the resolution
206 matrix shown here give us confidence in the significance and resolution of the obtained
207 anisotropy.

4.2. Results

208 The obtained phase velocity maps are shown in Figure 13 for periods of 18 s, 44 s, and
209 85 s. The results reveal lateral variations in isotropic phase velocities at all periods,
210 consistent with the presence of a flat slab: phase velocities are generally larger than
211 average in the forearc, and lower than average near the TMVB. At short periods (16 s-
212 33 s), there are strong lateral variations in phase velocities and anisotropy. Considering the
213 depth sensitivity of Rayleigh waves at these periods (see sensitivity kernels in Figure 14),
214 these rather complex variations may reflect changes in the crustal and mantle lithospheric
215 structure, and deformation history. At periods of 38 s and higher, the phase velocity
216 anomalies and anisotropy are smoother. It is remarkable to note that the transition
217 between the faster and slower than average phase velocities follows the isodepth lines of
218 the local seismicity, both in the flat and steeper portions of the slab.

219 We also find an east-west variation in phase velocity anisotropy at all periods, and a
 220 change in the fast direction between the forearc and the backarc. Both findings are likely
 221 to be the signature of complex 3-D deformation at depth. Interestingly, at periods of
 222 38 s and higher, the fast direction of propagation in the western part of our study region
 223 is perpendicular to the trench near the coast. In the southeast, the fast direction found
 224 above the slab is subparallel to the trench at most periods. In the backarc, azimuthal
 225 anisotropy is present at all periods up to 85 s, with the fast direction of propagation often
 226 at a steep angle to the strike of the arc. Considering that at periods larger than 33 s
 227 our data are mostly sensitive to structure below 50 km depth (Figure 14), and considering
 228 previous estimates of the slab geometry from body wave data (*Husker and Davis, 2009*),
 229 the orientation of the fast direction likely reflects lithospheric and/or asthenospheric de-
 230 formation.

5. Three-dimensional models

5.1. Shear-wave velocity structure

231 Phase velocities provide only a depth-integrated image of the upper mantle. In order
 232 to obtain a 3-D model, we need to invert the phase velocity maps for shear wave velocity
 233 and anisotropy.

Perturbations in the isotropic part of the phase velocity c_0 correspond to the depth average of perturbations in shear-wave velocity (δV_S), P-wave velocity (δV_P), and density ($\delta\rho$) weighted by sensitivity kernels (Figure 14):

$$\delta c_0 = \int_0^a [K_{V_S}(r)\delta V_S(r) + K_{V_P}(r)\delta V_P(r) + K_\rho(r)\delta\rho(r)]dr \quad (8)$$

234 where a represents the radius of the Earth, and $K_m(r)$ is the phase velocity sensitivity
235 kernel or partial derivative with respect to model parameter m (here m stands for V_S , V_P ,
236 and ρ).

237 In this work, the isotropic part of the phase velocity maps is inverted for V_S via a lin-
238 earized least-squares inversion using code *surf96* (Herrmann, 1987; Herrmann, Ammon,
239 2002). We impose a depth parameterization in terms of three layers down to 200 km depth,
240 with the top layer representing the crust and the other two layers being located in the
241 mantle (Figure 15D). The middle layer spans depths going from the Moho, as constrained
242 by receiver function analyses (see explanations below), to 100 km depth. Like most geo-
243 physical inverse problems, inversions of surface wave phase velocities to constrain V_S are
244 inherently non-unique. Part of the non-uniqueness arises from the existence of trade-
245 offs between the Moho depth and velocity structure. Therefore, to reduce the number of
246 models that can explain the data, and because receiver function analyses are better suited
247 than surface waves to constrain crustal thickness, we impose a priori constraints on the
248 Moho depth based on the work by *Kim and Clayton* (personal communication). Since the
249 Moho depths are only determined where seismic stations are located, we interpolate the
250 data where no receiver function information is available. The Moho depth is thus laterally
251 variable and so is the thickness of the two top layers of the model. The initial values of
252 density and V_P for the inversion are assigned based on the reference model mTNA (Ta-
253 ble 1); for each layer of our model (Figure 15D), we average the values from mTNA within
254 the same depth range. During the inversion, the V_P/V_S ratio is kept fixed.

255 Herrmann's method uses differential smoothing during the inversion, which means that
256 it damps the differences between V_S in adjacent layers. After investigating a range of

257 values for the damping parameter, we choose to start with the damping of 10% of the
 258 maximum eigenvalue of the data kernel, decreasing it to 3% after five iterations in the
 259 total of 30 iterations. The selection of the damping values and number of iterations is
 260 based on the final solution stability and improvement in misfit.

261 The depth inversions are carried out at every grid cell that parametrizes the study area
 262 (section 4), and the resulting shear-wave velocity profiles are combined to form a 3-D V_S
 263 model of the region as displayed in Figure 15. Our model shows lateral variations in V_S at
 264 all depths, with larger values in the south of the study region, most likely reflecting the
 265 presence of the slab, and slightly lower in the northern part of the region. We find lateral
 266 variations in V_S of approximately 0.3 km/s in the mantle and crust. Note that, since
 267 our 3-D V_S model results from the inversion of phase velocity maps that are themselves
 268 generated by inversion of dispersion measurements, our V_S model amplitude is indirectly
 269 affected by the smoothing applied during the construction of the phase velocity maps. A
 270 lower damping of the shortest period dispersion data may have resulted in stronger phase
 271 velocity anomalies and stronger crustal V_S .

5.2. Azimuthal anisotropy

At a given period T , the phase velocity azimuthal anisotropy relates to azimuthal anisotropy at depth through equations similar to Eq. 8:

$$c_1 = \int_0^a K_G G_c dr \quad (9)$$

$$c_2 = \int_0^a K_G G_s dr \quad (10)$$

272 where c_1 and c_2 are the 2Ψ anisotropic terms of Eq. 2, G_c and G_s are elastic parameters that
 273 describe the azimuthal anisotropy of vertically polarized shear-waves, and K_G describes
 274 the sensitivity of Rayleigh waves to G_c and G_s .

275 We invert Eqs. 9 and 10 for $G_c(r)$ and $G_s(r)$ using a singular value decomposition (SVD)
 276 method. We follow the procedure described by *Matsu'ura and Hirata* (1982) to determine
 277 how many eigenvalues to keep in the reconstruction of the model. The inversion is done
 278 over the same layers used for the inversion of the isotropic term. After obtaining a model
 279 for G_s and for G_c , we calculate the amplitude A of the anisotropy and the fast direction
 280 of propagation Θ for vertically polarized shear-waves at every grid cell and in every layer
 281 using :

$$A = \sqrt{(G_c^2 + G_s^2)} \quad (11)$$

$$\Theta = 1/2 \arctan(G_s/G_c) \quad (12)$$

282 The results are displayed in Figure 15. In our interpretation, we concentrate on the pat-
 283 terns in the mantle lithosphere and asthenosphere (Figure 15B,C). Unlike most subduction
 284 zones that display anisotropy with the fast direction parallel to the trench (*Long and Sil-*
 285 *ver*, 2008), our results show a more complex pattern of anisotropy, with the fast azimuth
 286 of propagation perpendicular to the trench northwest of MASE and almost parallel to the
 287 trench in the southeast (Figure 15B, C). There is a clear and sharp near-vertical transi-
 288 tion between 45 and 200 km depth showing 0.5-2% variations in anisotropy with higher
 289 amplitudes where the fast direction is parallel to the trench. In the crust (Figure 15A), we

290 observe a complex anisotropy pattern. Overall, the crustal anisotropy does not coincide
291 with that of either mantle lithosphere (Figure 15B) or asthenosphere (Figure 15C). This
292 is not surprising, since anisotropy at different depth likely has different origins (Lin et
293 al., 2010; Yang et al., 2011): the anisotropy in the crust correlates with geologic/tectonic
294 features whereas the anisotropy in the upper mantle depends on temperature variations
295 and mantle flow. A similar variation in anisotropic behavior with depth is also observed
296 in the western United States (Lin et al., 2010; Yang et al., 2011).

297 Our anisotropy results combined with our S-wave velocity model enable us to obtain
298 new insights into the Mexico subduction zone, as discussed in the next section.

6. Discussion

6.1. Evidence for tear in the slab along OFZ

299 Our results confirm the conclusions of prior studies (*Kanjorski, 2003; Pardo and Suarez,*
300 *1995; Blatter et al., 2007*) that the angle of subduction varies substantially along the
301 trench. There are several distinctive features observed with V_S that vary gradually be-
302 tween layers in Figure 15D. The higher velocities of 4.4 km/s are seen in the middle layer
303 (Figure 15B) in the subduction zone near the coast, extending inland beneath the southern
304 part of the MASE array. We associate these higher velocities with the slab subduction,
305 specifically with a shallow flat slab under the MASE and a steep slab to the west of it.
306 This finding is consistent with the shallow slab location determined by *Pardo and Suarez*
307 *(1995), Perez-Campos et al. (2008), Husker (2008), and Husker and Davis (2009)* based on
308 seismicity patterns, receiver function tomography, and P-wave tomography, respectively.
309 The slabs at the depths of up to 100 km appear to be almost disconnected.

310 Another striking feature is a low velocity zone in the northern part of the MASE array
311 (Figure 15B), with a velocity contrast of 0.3 km/s between the low and high velocity
312 regions. We attribute the velocity reduction to the presence of water or melt in a mantle
313 wedge as a consequence of the subduction process. It is interesting to note that the low
314 velocity area almost coincides with the location of volcanoes from the TMVB. The results
315 for the bottom layer located between 100 and 200 km depth, (Figure 15C), exhibit a low
316 velocity zone in the northern part of the MASE array and an absence of the high shear
317 velocities associated with the flat slab beneath the southern part of the MASE array. This
318 can be explained by the fact that the flat part of the slab is mostly absent at this depth
319 and its steeply dipping part at 74° is not detectable by the surface waves since it is quite
320 thin as was shown by the P-wave tomography (*Husker and Davis, 2009*). On the other
321 hand, the mantle wedge to the north is much wider and more detectable by Rayleigh
322 waves and corresponds to a low velocity area. The asthenospheric low velocities beneath
323 the TMVB are likely caused by altered mantle due to slab dehydration and/or increase in
324 temperature in the mantle wedge. Although the slab itself is not visible as a high velocity
325 zone, the transition to the low velocities in the north can also be used for locating the
326 slab.

327 Higher velocities are seen to the west of the MASE array. This is probably explained
328 by the large detectable size of the steeply dipping slab that crosses this zone. We note
329 that the isodepth line at 120 km depth runs on the edge of the blue region supporting
330 the presence of the slab. The low velocity zone to the northwest of the steep slab is close
331 to the boundary of our well-resolved area and hence potentially suspect, but it can be

332 associated with a possible signature of the mantle wedge associated with subduction of
333 the Rivera slab as mentioned in *Yang et al.* (2009).

334 We can thus observe that the subducting slab in the study area is separated into two
335 sections, one of which is flat and shallow (section 3, Figure 1) while the other one is steep
336 and deep (section 2, Figure 1). An important issue is how the subduction changes across
337 the boundary between the flat and steep portions. One possibility is that the slab is
338 continuous, experiencing relative rapid but continuous change in subduction angle (Fig-
339 ure 16, bottom). Such a scenario was hypothesized by *Pardo and Suarez* (1995). However,
340 our results on anisotropy, combined with prior studies on the ocean plate structure, age
341 and convergence rates, as well as the slab rollback and retreat (*Mori et al.*, 2007; *Orozco*
342 *et al.*, 2007; *Manea et al.*, 2005), point towards the scenario with a tear in the slab, as
343 illustrated in Figure 16 (top). Note that the study area is rotated in Figure 16 relative to
344 that of Figures 13 and 15, to give a better view of the slab morphology. The location of
345 the transition from steep (B) to shallow (A) subduction is consistent with the location
346 of the Orozco Fracture Zone (OFZ), which separates the older, cooler and denser oceanic
347 crust (17.6 Ma old) from the younger oceanic crust and lithosphere (12.3 Ma old) (*Manea*
348 *et al.*, 2005; *Pardo and Suarez*, 1995).

349 The existence of the tear is further supported by our anisotropy results. The fast
350 directions in the mantle lithosphere and asthenosphere are, in general, parallel to the
351 trench, except near the OFZ. In the vicinity of the OFZ they rotate to become near-
352 parallel with the OFZ projected path, eventually deviating slightly to the west (Figure 15B
353 and 15C). One of most likely causes of anisotropy is the flow-induced, lattice-preferred
354 orientation of olivine. This theory is supported by a study based on P wave tomography

355 results (*Yang et al., 2009*) that describes the mantle flow between our steep slab (B) and
356 the Rivera slab (C) as caused by an existence of a gap between the Rivera and Cocos.
357 Studies on GPS velocities (*DeMets et al., 1994*) and volcanic migration (*Blatter et al.,*
358 *2007*) suggest that slab retreat and/or rollback are occurring at 5 cm/year in our study
359 area. The rollback/retreat should displace mantle asthenosphere and, in the presence of
360 the slab tear, the mantle material would flow through it. The associated toroidal flows
361 (Figure 16, top, blue arrows) would give rise to the anisotropy pattern obtained in our
362 study (Figure 15b and 15c). The "currents" meet in front of the steep slab B, creating a
363 characteristic line. This is similar to the explanation of the circular pattern of anisotropy
364 in the Western US given by *Zandt and Humphreys (2008)*. Note that the flow between
365 segments A and B may also contribute to the flatness of subduction, dynamically elevating
366 the flat slab section. We conclude that the A-B tear occurs where the plate is weakened
367 by the presence of the fracture zone. In the back arc, the steep angle of mantle anisotropy
368 to the strike of the arc can be explained by the flow in the mantle wedge (Figure 16, top,
369 green arrows).

6.2. Implications for the geometry of the TransMexican Volcanic Belt (TMVB)

370 It is commonly pointed out that TMVB is oblique to the trench (*Ferrari, 2004; Pardo*
371 *and Suarez, 1995*). The slab model with the tear allows for an alternative interpretation
372 of TMVB as a combination of two segments both of which are parallel to the trench
373 (Figure 17). One segment of the volcanic belt (B' in Figure 17) is generated by the steeper
374 portion of the slab (B in Figure 17), and hence it is located closer to the trench. The other
375 segment (A') is generated by the flatter portion of the slab and hence it is farther from the

376 trench. Each of the segments of the volcanic belt is parallel to the trench, consistent with
377 typical understanding of the subduction zone volcanism (*Mori et al.*, 2007). However, the
378 difference in their distance to the trench results in what appears to be an oblique angle
379 between the TMVB, taken as a whole, and the trench. Note that the oblique character of
380 TMVB has already been linked to the changing subduction angle by prior studies (e.g.,
381 *Pardo and Suarez*, 1995). However, what is new in our results is the possibility that the
382 TMVB is actually segmented.

383 This new interpretation allows for a natural explanation for the existence of the Tzitzio
384 gap in volcanism (e.g., *Blatter et al.*, 2007). The gap occurs right on top of the projected
385 path of the OFZ, and hence on top of the proposed tear in the slab structure. In this
386 interpretation, the Tzitzio gap is simply the result of the two parallel segments that are
387 displaced with respect to each other, as illustrated in Figure 17. The zone between them
388 does not have steeply subducted material that would generate volcanism.

7. Conclusions

389 To investigate the structure of the Mexican subduction zone, we have constructed
390 Rayleigh wave phase velocity maps, included the effect of the anisotropy, and inverted
391 the results for the 3D structure of the zone in terms of shear wave velocities and their
392 anisotropy. This detailed analysis has been possible due to the high density of stations.

393 The lateral variations in the isotropic part of the velocity structure in the mantle litho-
394 sphere point to the different styles of subduction on the two sides of the OFZ, with steep
395 subduction to the northwest and nearly flat subduction to the southeast. This finding is
396 consistent with previous studies of the structure using different methods (*Husker*, 2008;
397 *Perez-Campos et al.*, 2008; *Iglesias et al.*, 2010; *Orozco et al.*, 2007) as well as with the

398 two parts of the slab having different ages and hence different densities (*Blatter et al.*,
399 2007; *Kanjorski*, 2003; *Manea et al.*, 2006). The deeper, asthenospheric layer reveals lower
400 velocities below the TMVB, presumably due to dehydration effects.

401 The anisotropy pattern is consistent with a tear between the two styles of subduction,
402 along the OFZ, a tear between the steep Cocos and Rivera slabs, and with the associated
403 toroidal return flows through the tears and around the steeply dipping section of the Cocos
404 slab. This conclusion is supported by the gradual variation of the fast directions from
405 trench-parallel near the trench to trench-perpendicular inland west of the OFZ. The flows
406 could be caused by the slab rollback/retreat evidenced by GPS velocities and migration
407 of TMVB (*DeMets et al.*, 1994; *Manea et al.*, 2005; *Mori et al.*, 2007).

408 Our hypothesis that the slab is torn allows for a new insight into the structure of the
409 TMVB. The TMVB can be interpreted as consisting of two segments (A and B) associated
410 with the two parts of the torn slab. Each segment is parallel to the trench, as commonly
411 found in subduction zones. However, the two TMVB segments are located at different
412 distances from the trench, consistent with the different angles of subduction. This creates
413 an apparent oblique orientation of the TMVB. The segmented structure of the TMVB
414 also provides a natural explanation for the Tzitzio gap in volcanism, which is located on
415 top of the OFZ, where the two proposed TMVB segments are shifted with respect to each
416 other.

417 **Acknowledgments.** We thank S. Lebedev of Dublin Institute for Advanced Studies,
418 Dublin, Ireland who provided software package used to calculate the phase velocity model,
419 and J. Arthur Snoke of Virginia Tech for the two-station method code. Map figures were
420 constructed using GMT software (*Wessel and Smith*, 1998). Waveform data were provided

421 by the IRIS DMC, MASE, MARS, and NARS projects. The funding was provided by the
422 Tectonics Observatory at Caltech, the Center for Embedded Network Sensors (CENS) at
423 UCLA, NSF award EAR0609707, PAPIITUNAM projects IX120004 and IN119505-3, and
424 UC MEXUS project 04105384. The MASE experiment was funded by the Gordon and
425 Betty Moore Foundation.

References

- 426 Atwater, T., and J. Stock, 1998. Pacific North America plate tectonics of the Neogene
427 southwestern United States: An update, *Int. Geol. Rev.*, 40, 375-402.
- 428 Backus, G., 1970. A geometrical picture of anisotropic elastic tensors. *Reviews of geo-*
429 *physics*, 8(3), 633-671.
- 430 Bassin, C., Laske, G. and Masters, G., 2000. The Current Limits of Resolution for Surface
431 Wave Tomography in North America, *EOS Trans AGU*, 81, F897.
- 432 Beghein, C., Snoke, J.A., and Fouch, M.J., 2010. Depth Constraints on Azimuthal
433 Anisotropy in the Great Basin from Rayleigh Wave Phase Velocity Maps, *Earth Planet.*
434 *Sci. Lett.*, 289, 467-478.
- 435 Bevington, P.R., Robinson, D.K., 1992. Data Reduction and Error Analyses for the Phys-
436 ical Sciences *McGrow-Hill, New-York*.
- 437 Blatter D., Farmer G., Carmichael I., 2007. A North-South Transect across the Central
438 Mexican Volcanic Belt at 100°W: Spatial Distribution, Petrological, Geochemical, and
439 Isotopic Characteristics of Quaternary Volcanism, *Journal of Petrology*, 48, 901-950.
- 440 Brune, J., and J. Dorman, 1963. Seismic waves and earth structures in the Canadian
441 shield, *Bull. Seismol.Soc.Am.*, 53, 167-210.

- 442 Chen, T., and R. W. Clayton, 2009. Seismic attenuation structure in central Mexico:
443 Image of a focused high-attenuation zone in the mantle wedge, *J. Geophys. Res.*, 114,
444 B07304.
- 445 Crampin, S., Chesnokov, E. M., Hipkin, R., 1984. Seismic anisotropy; the state of the art,
446 II, *Geophysical Journal of the Royal Astronomical Society* , vol.76, no.1, pp.1-16.
- 447 Darbyshire, F. A., Lebedev, S., 2009. Rayleigh wave phase-velocity heterogeneity and
448 multi-layered azimuthal anisotropy of the Superior Craton, Ontario, *Geophys. J. Int.*,
449 176 (1), 215-234.
- 450 DeMets, C., R. G. Gordon, D. F. Argus, and S. Stein, 1994. Effect of recent revisions
451 to the geomagnetic reversal time-scale on estimates of current plate motions, *Geophys.*
452 *Res. Lett.*, 21, 2191-2194.
- 453 Dziewonski, A., Bloch, S., Landisman, N., 1969. A technique for the analysis of transient
454 seismic signals. *Bull. Seism. Soc. Am.*, 59, 427-444.
- 455 Ferrari, L., 2004. Slab detachment control on mafic volcanic pulse and mantle heterogene-
456 ity in central Mexico, *Geology*, 32(1), 77-80.
- 457 Grand, S. P., Helmberger, D., 1984. Upper mantle shear structure of North America.
458 *Geophysical Journal of the Royal Astronomical Society*, vol.76, no.2, 399-438.
- 459 Herrmann, R., 1987. Computer programs in seismology. *Tech. rep. St. Luis University*,
460 St. Luis, Missouri.
- 461 Herrmann, R., Ammon, C., 2002. Computer programs in seismology. *Tech. rep. St. Luis*
462 *University*, St. Luis, Missouri.
- 463 Husker, A. L., 2008. Tomography of the subducting Cocos Plate in central Mexico using
464 data from the installation of a prototype wireless seismic network: Images of a truncated

- 465 slab, *Ph.D. thesis*, 107 pp., Univ. of Calif., Los Angeles.
- 466 Husker, A., Davis, P., 2009. Tomography and thermal state of the Cocos plate subduction
467 beneath Mexico City, *J. Geophys. Res.*, Vol. 114, No. B4, B04306.
- 468 Husker A., Stubailo I., Lukac M., Naik V., Guy R., Davis P., Estrin D., 2008. WiLSoN: The
469 Wirelessly Linked Seismological Network and its application in the Middle American
470 Subduction Experiment, *SRL* .
- 471 Iglesias, A., R. Clayton, X. Perez-Campos, S. K. Singh, J. Pacheco, D. Garcia, and C.
472 Valdes-Gonzalez, 2010. S-Wave, Velocity Structure below Central Mexico using High
473 Resolution Surface Wave Tomography, *J. Geophys. Res.*, 115, B06307.
- 474 Kanjorski M., 2003. Cocos Plate structure along the Middle America subduction zone off
475 Oaxaca and Guerrero, Mexico: influence of subducting plate morphology on tectonics
476 and seismicity, PhD thesis, University of California, San Diego.
- 477 Karato S., 1998. Seismic anisotropy in the deep mantle, boundary layers, and the geometry
478 of mantle convection, *Pageoph* 151, 565-587.
- 479 Kennett B. L. N., Engdahl E. R., Buland R., 1995. Constraints on seismic velocities in
480 the Earth from traveltimes, *Geophys. J. Int.*, vol.122, no.1, 108-124.
- 481 Kim, Y., Greene, F., Espejo, L., Perez-Campos, X., Clayton, R., 2006. Receiver function
482 analysis of the Middle American subduction zone in central Mexico, *EOS, American*
483 *Geophysical Union*, vol. 87.
- 484 Knopoff L., Berry M. J, Schwab F. A., 1967. Tripartite phase velocity observations in
485 laterally heterogeneous regions. *Journal of geophysical research*, 72(10), 2595-2601.
- 486 Landisman, N., Dziewonski, A., Sato, Y., 1969. Recent improvements in the analysis of
487 surface wave observations. *Geophysical Journal of the Royal Astronomical Society*, vol.

488 4, 369-403.

489 Lin, F., Ritzwoller M. H., Yang Y., Moschetti M. P., Fouch M. J., 2011. Complex and
490 variable crustal and uppermost mantle seismic anisotropy in the western United States.

491 *Nature Geoscience*, 4, 5561 (2011)

492 Lonsdale, P., 1991. Structural pattern of the Pacific floor offshore peninsular California,
493 in Dauphin, J.P., and Simoneit, B.R.T. eds., The Gulf and Peninsular Province of the
494 Californias. *American Association of Petroleum Geologists*, Memoir 47, 87-125.

495 Long, M. D., and P. G. Silver, 2008. The subduction zone flow field from seismic
496 anisotropy: A global view, *Science*, 319, 315-318, doi:10.1126/science.1150809.

497 Manea, V., M. Manea, V. Kostoglodov, and G. Sewell, 2006. Intraslab seismicity and
498 thermal stress in the subducted Cocos plate beneath central Mexico, *Tectonophysics*,
499 420, 389-409.

500 Manea, M., V. Manea, Luca Ferrari, V. Kostoglodov, and W. Bandy, 2005. Tectonic
501 evolution of the Tehuantepec Ridge, *EPSL*, 238, 64-77.

502 Mann, P., 2007. Global catalogue, classification and tectonic origins of restraining- and
503 releasing bends on active and ancient strike-slip fault systems, *Geol. Soc. London, Sp.*
504 *Publ.*, 290.

505 Matsu'ura, M., and Hirata, N., 1982. Generalized least-squares solutions to quasi-linear
506 inverse problems with a priori information, *J. Phys. Earth*, 30, 451-468.

507 Mori, L, Gomez Yuena, A., Cai, Y., Goldstein, S.T., 2007. Effects of prolonged flat sub-
508 duction on the Miocene magmatic record of the central Trans-Mexican volcanic belt.
509 *Chemical geology*, 244(3-4), 452-473.

- 510 Orozco Esquivel, T., Petrone, C. M., Ferrari, L., Tagami, T., Manetti, P., 2007. Geochem-
511 ical and isotopic variability in lavas from the eastern Trans-Mexican volcanic belt; slab
512 detachment in a subduction zone with varying dip. *Lithos*, 93(1-2), 149-174.
- 513 Pardo, M., and Suarez G., 1995. Shape of the subducted Rivera and Cocos plates in
514 southern Mexico: Seismic and tectonic implications, *J. Geophys. Res.*, 100, 12,357-
515 12,373.
- 516 Perez-Campos, X., Kim, Y., Husker, A., Davis, P. M., Clayton R. W., Iglesias A., Pacheco
517 J. F., Singh S. K., Manea V. C., and Gurnis M., 2008. Horizontal subduction and and
518 truncation of the cocos plate beneath Central Mexico, *Geophys. Res. Lett.*, 35, L18303.
- 519 Sato, Y., 1955. Analysis of dispersed surface waves by mean of Fourier transform: Part I,
520 *Bull. Earthquake Res. Tokyo Univ.*, 33, 33-47.
- 521 Silver, P. G., 1996. Seismic anisotropy beneath the continents: probing the depths of
522 geology., *1081 Annu. Rev. Earth Planet. Sci.*, 24, 385-432.
- 523 Smith, M. L., Dahlen, F. A., 1973. The Azimuthal Dependence of Love and Rayleigh
524 Wave Propagation in a Slightly Anisotropic Medium, *J. Geophys. Res.*, vol.78, no.17,
525 3321-3333.
- 526 Stubailo, I., Davis P., 2007. Shear wave splitting measurements and interpretation beneath
527 Acapulco-Tampico transect in Mexico, *AGU presentation*.
- 528 Trampert, J., Woodhouse, J., 2003. Global anisotropic phase velocity maps for fundamen-
529 tal mode surface waves between 40 and 150 s., *Geoph. J. Int.*, 154, 154-165.
- 530 Truchan M., Larson R., 1973. Tectonic lineaments on the Cocos Plate, *EPSL*, 17, 46-432.
- 531 Warren, L., Snoke, J., James, D., 2008. S-wave velocity structure beneath the High Lava
532 Plains, Oregon, from Rayleigh-wave dispersion inversion, *Earth Planet. Sci. Lett.*, 274,

533 121-131.

534 Wilson, D., 1996, Fastest known spreading on the Miocene Cocos-Pacific plate boundary,
535 *Geophysical Research Letters*, v. 23, 3003-3006.

536 Wessel, P., and W. H. F. Smith, 1998. New, improved version of the Generic Mapping
537 Tools released, *Eos Trans. AGU*, 79, 49, 579.

538 Yang, Z., Sheehan, A., Shearer P., 2011. Stress-induced upper crustal anisotropy in south-
539 ern California, *J. Geophys. Res.*, vol. 116, B02302, doi:10.1029/2010JB007655.

540 Yang, T., Grand, S. P., Wilson, D., Guzman-Speziale, M., Gomez-Gonzalez, J. M.,
541 Dominguez-Reyes, T., and Ni, J., 2009. Seismic structure beneath the Rivera sub-
542 duction zone from finite-frequency seismic tomography, *J. Geophys. Res.*, vol.114,
543 doi:10.1029/2008JB005830.

544 Zandt, G., Humphreys, E., 2008. Toroidal mantle flow through the Western U.S. slab
545 window. *Geology*, 36(4), 295-298.

Figure 1. Tectonic setting of the region. The area imaged in this study is centered under the MASE array, which stretches from Acapulco to Tempoal. The MASE stations and other stations that fall within the map area are shown as triangles. The Middle America Trench (MAT), East Pacific Rise (EPR), Orozco Fracture Zone (OFZ) are also displayed. The circles represent the volcanoes that are part of the Trans-Mexican Volcanic Belt (TMVB). The isodepth lines of the Wadati-Benioff zone obtained from the local seismicity tell us that the slab is steeper in the North-West than in the South-East, and that the slab under the southern half of the MASE array is relatively flat. The circled numbers indicate the four sections of the slab geometry: Jalisco (1), Michoacan (2), Guerrero-Oaxaca (3), Oaxaca (4) from *Pardo and Suarez (1995)*.

Figure 2. 2-D view of the slab under the MASE array based on P-wave tomography (*Husker, 2008*) and receiver function analysis (*Perez-Campos, 2008*). (A) Map view of the area showing the slab and the MASE array above it. Note the dense positioning of stations. (B) The location of the study area with respect to the trench. The study area lies within section 3 of *Pardo and Suarez (1995)*. (C) The side view of the slab. The subducting slab is nearly flat for 230-250 km, and then bends relatively abruptly below the middle of the MASE array, with the subducting angle of 74° . The slab truncates at 520 km depth.

Figure 3. Seismic stations used in the study (triangles). The ray coverage is shown by grey lines. The area of best coverage is outlined by a blue rectangle. The circles indicate volcanoes.

Figure 4. Representative events (red stars) used for the study and the corresponding great circle paths (grey lines) connecting them to a MASE array station. The chosen earthquakes are shallower than 250 km and of magnitude $M \geq 6.0$ to have suitable signal-to-noise ratios. The events occurred between 2005/01/14 and 2009/11/13.

Figure 5. FTAN plots (*Landisman et al.*, 1969; *Dziewonski et al.*, 1969) showing single-station Rayleigh-wave group velocities *vs.* periods for the 1 March 2007 event (middle of the North Atlantic Ocean). The X symbols are computer-picked energy maxima for each period, the vertical lines span ± 1 dB. Contours are placed every 3 dB. The corresponding waveforms are shown on the right sides. Panel (A) gives an example of a smooth FTAN plot for station SCIG that was used for data processing, and panel (B) shows an irregular FTAN plot for station VENA which was rejected. In (B), the contours are not smooth and well-behaved over all periods.

Figure 6. One-dimensional shear wave velocity profile used as a local reference Earth model. It is a composite model modified from the Tectonic North America (TNA) model (*Grand and Helmberger*, 1984) with the added P-wave velocities and densities from model AK135 (*Kennett et al.*, 1995), and the Crust 2.0 crustal model (*Bassin et al.*, 2000).

Table 1. Modified Tectonic North America model (mTNA). Figure 6 illustrates the V_S velocity profile of this model.

Figure 7. Dispersion curves along the MASE transect for three pairs of stations: (a) CARR and ESTA, located right above the slab, (b) PSIQ and PLAT, located only partially above the slab, and (c) IXCA and PLIG, located away from the slab. The location of the slab is assumed based on previous 2-D studies (e.g. *Husker and Davis (2009)*). The black dots and vertical lines give the interstation phase velocities and uncertainties measured by the two-station method. The solid lines indicate the dispersion curves predicted by the 1-D modified Tectonic North America model (mTNA). Note the systematic differences between the dispersion curves, both in terms of their departure from the 1-D model and in terms of their variation along the transect. The phase velocities above the slab are larger, and diminish while moving away from the slab, as we would expect.

Figure 8. L-curves (trade-off curves) for the periods of 18, 22, 28, 38, 54, and 85 s. The L-curve displays a measure of the misfit of each model against a measure of the complexity of the model itself (damping). The dots show the points used as damping values for the preferred model; they differ for different periods.

Figure 9. An example of reduced χ^2 as a function of the trace of \mathbf{R} for the isotropic (squares), isotropic and 2Ψ inversions (circles), and isotropic and full anisotropy of $2\Psi + 4\Psi$ (triangles) for the period of $T=28$ s. The values for the χ^2 and trace are calculated for a range of damping parameters with the values of the preferred model marked by arrows. The dampings increase from right to left. We can see that the 4Ψ terms do not improve the fit significantly, and thus only isotropic and 2Ψ terms are used for anisotropic depth inversions.

Figure 10. Isotropic resolution test for $T = 44$ s. The comparison between the isotropic checkerboard input model (A) and the recovered isotropic phase velocity map (B) shows that the area around the MASE array (the non-shaded region) is well-resolved. The resolution near the MASE array is good due to the high number of the intersecting paths.

Figure 11. Anisotropic resolution tests for $T = 44$ s. Panels (A) and (B) correspond to anisotropic inversions of an isotropic input model, and panels (C) and (D) show anisotropic inversions of an anisotropic input model. The input models are shown to the left and the output models are represented on the right. The input model with zero anisotropy (A) is chosen to coincide with the isotropic component of our preferred model of the region.

Figure 12. Resolution matrix for 44 s period calculated using our chosen damping. The nine submatrices represent trade-offs between the isotropic terms of the phase velocity map c_0 , and the 2Ψ terms c_1 and c_2 of Eq. 2. The elements of each submatrix represent our 898 triangular grid cells. The off-diagonal submatrices indicate trade-offs between the isotropic and anisotropic terms and between the two anisotropic terms. The off-diagonal elements of the diagonal submatrices indicate lateral trade-offs, i.e. trade-offs within the isotropic or one anisotropic term at different geographic locations.

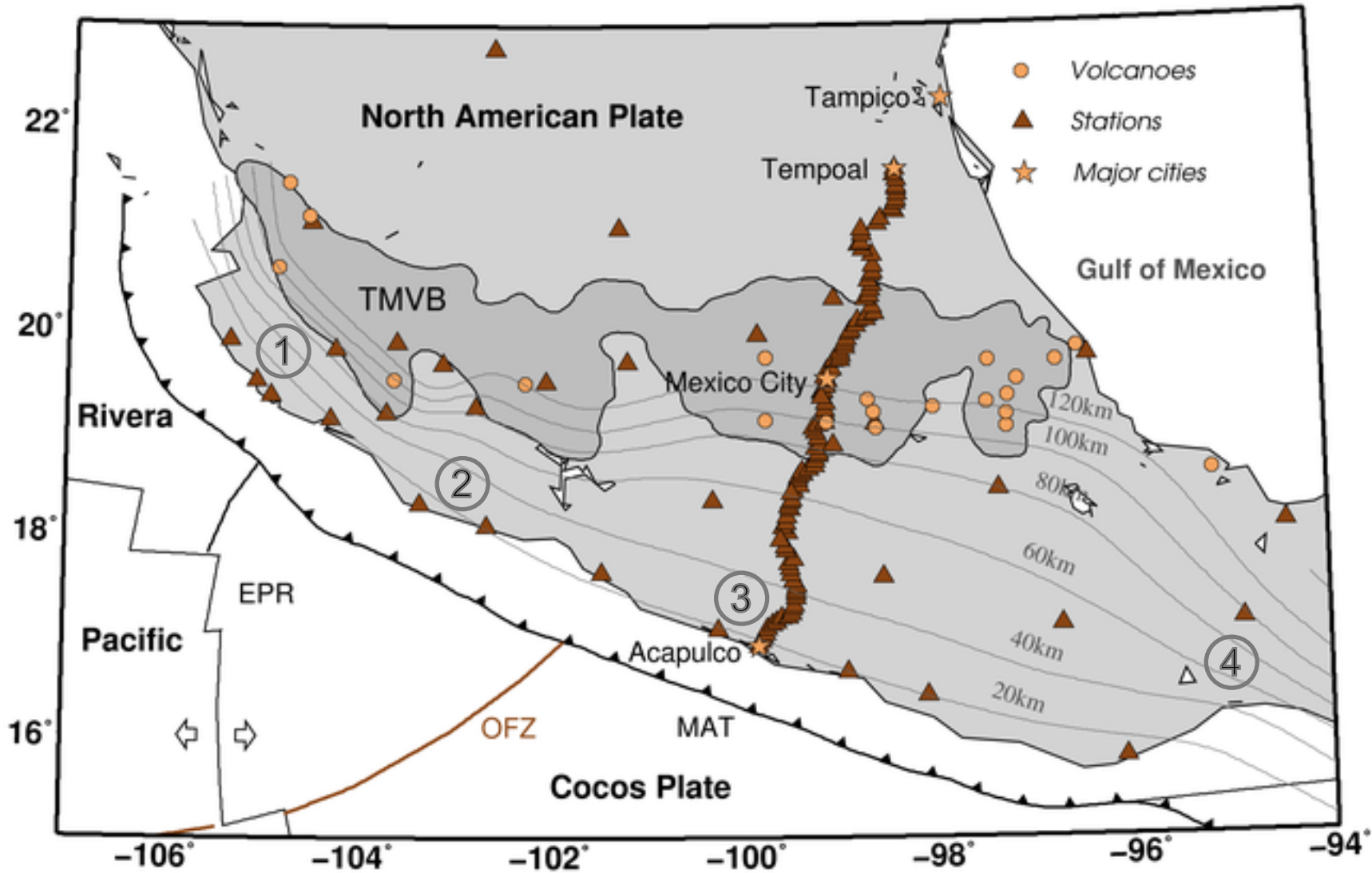
Figure 13. Anisotropic phase velocity maps for selected periods. The color scale represents deviations in isotropic phase velocity with respect to the phase velocity calculated for our local reference model mTNA. The red lines show both the fast direction and the magnitude of the 2Ψ -anisotropy. The non-shaded area (with the green semi-elliptical boundary) marks the well-resolved area as determined by the resolution test (Figure 10). The isolines of slab depth based on local seismicity are shown by grey lines as in Figure 1.

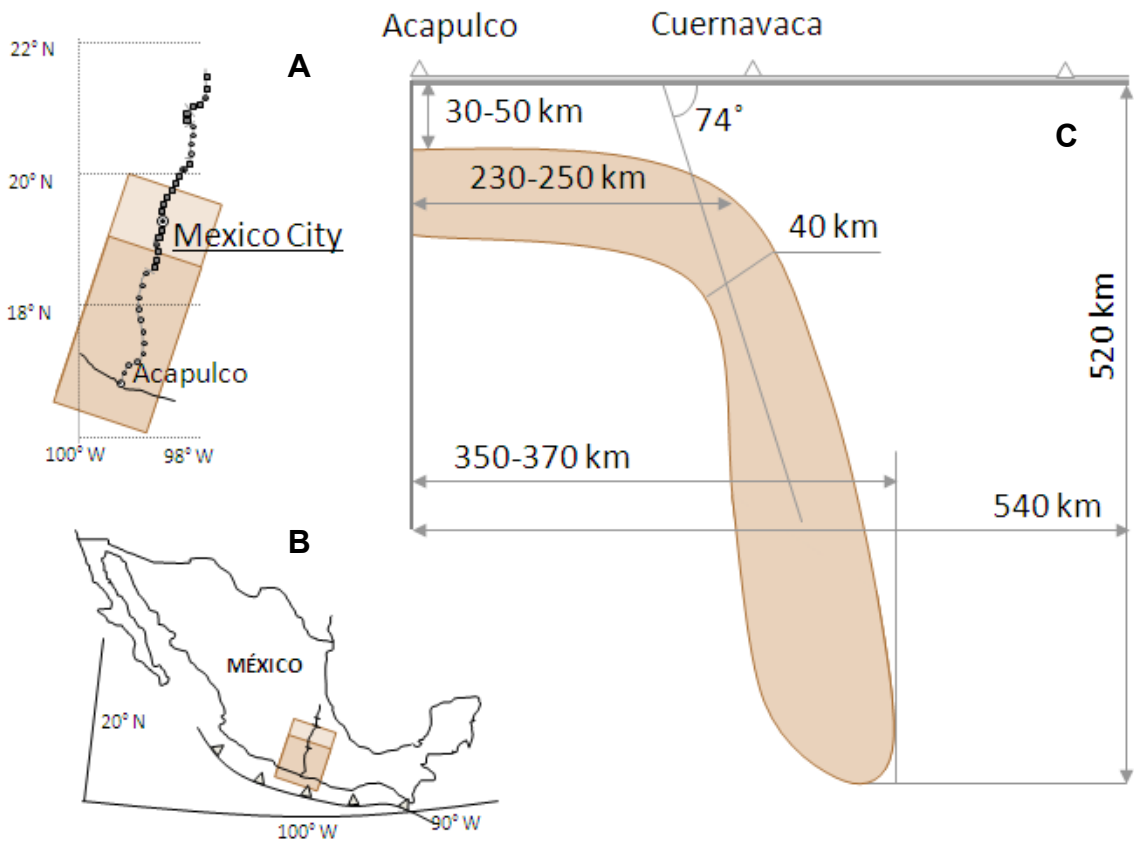
Figure 14. Sensitivity kernels for V_S as functions of depth for several of the different periods analyzed. The kernels are the partial derivatives for fundamental-mode Rayleigh wave phase velocities with respect to V_S based on the reference velocity model mTNA.

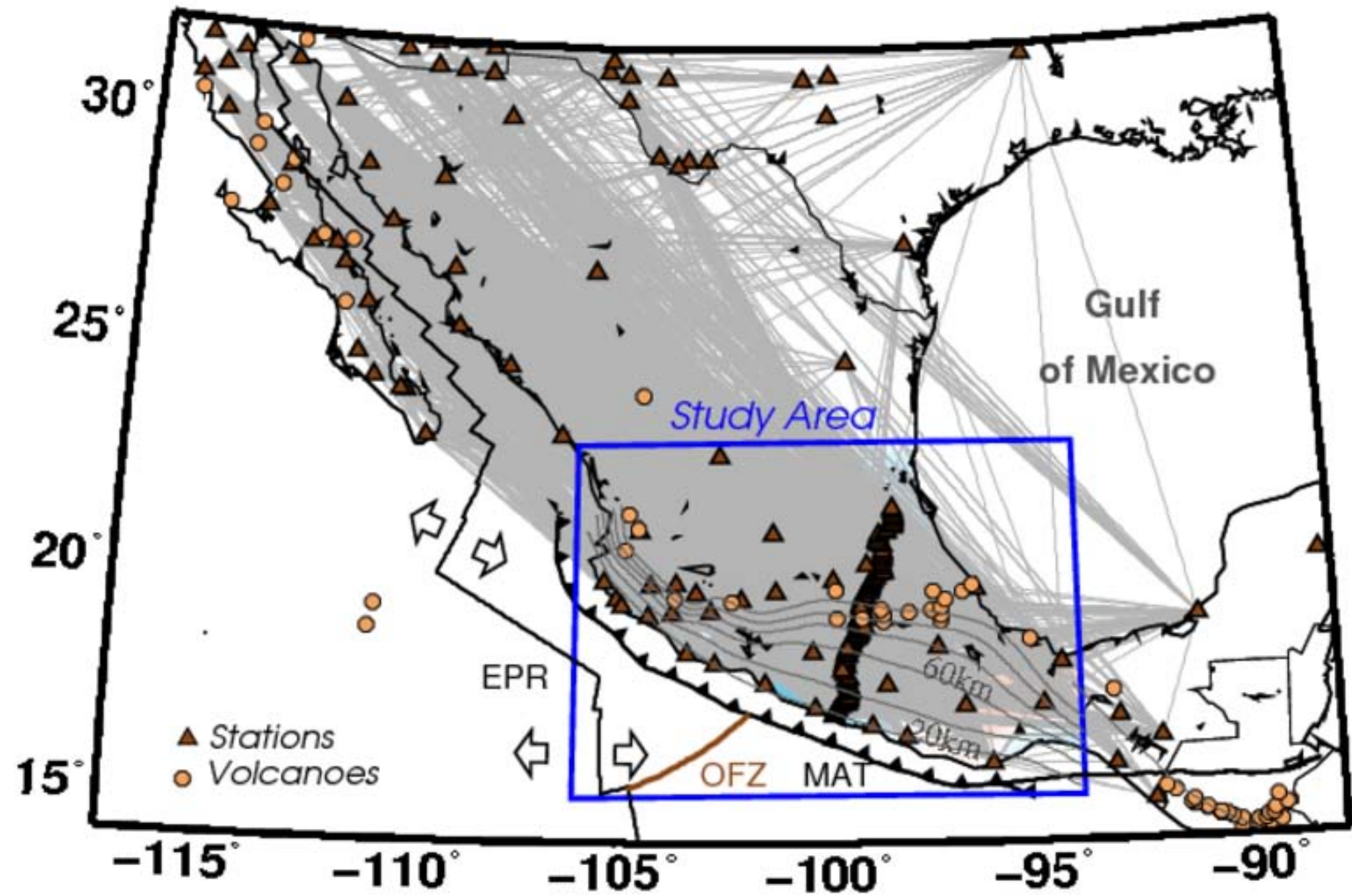
Figure 15. 3-D shear-wave velocity and anisotropy model based on the inversion of our Rayleigh wave phase velocity maps. (A-C) Shear-wave velocities (color) and fast directions (black dashes) averaged over each of the three layers of the model (D). Layers 1 and 2 have variable depth to account for lateral changes in crustal thickness. The velocity variations in the mantle lithosphere (layer 2) show high velocities in the subduction zone near the coast, extending inland beneath the southern part of the MASE array. These higher velocities are likely associated with the flat slab. Asthenospheric velocities (C) have low values beneath the TMVB, probably due to altered mantle from slab dehydration.

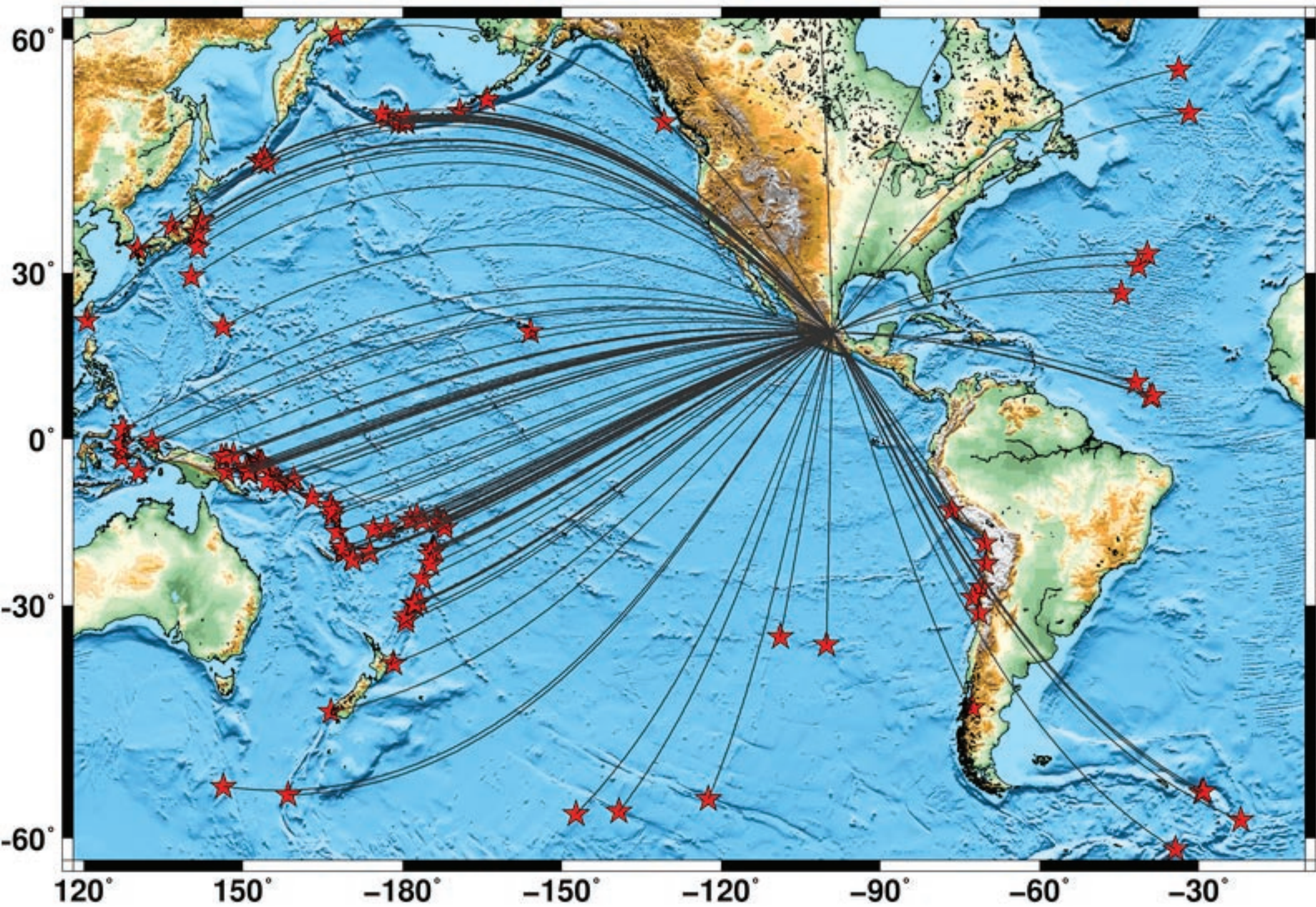
Figure 16. Two potential interpretations of the subduction structure in Mexico. *Top:* The flat (A) and steep (B) portions of the slab discussed in this paper separated by a tear. This is our preferred model that explains the anisotropy pattern (Figure 15). The slab retreat/rollback proposed for the area (Mori *et al.*, 2007) should displace the mantle asthenosphere, causing a toroidal flow through the tear and around the steep part of the slab (the blue arrow between A and B). The flow would explain the rotation of the fast direction in the anisotropy inversion. The tear between the two parts of the slab coincides with the projected path of the OFZ that separates the Cocos plate into areas of different ages. In addition, a mantle flow through the tear between the steep slab (B) and the Rivera slab (C) was observed in Yang *et al.*, (2009) based on P-wave tomography results. The converging flows from both sides of the steep slab B along with a wedge flow (green arrows), that has fast directions perpendicular to the trench in the back arc, explain the sharp change in the anisotropy direction line in front of the slab B (Figure 15). *Bottom:* The scenario in which the transition from the flat to steep subduction is continuous. In this scenario, the fast anisotropy direction perpendicular to the trench would be caused by the wedge flow which may be further enhanced by the slab retreat/rollback. This scenario does not explain the observed continuous rotation of the fast directions towards the OFZ that separates the two modes of subduction. *Insert:* The map view of the area with the locations of slab portions A, B, and C.

Figure 17. Interpretation of the TMVB structure as consisting of two trench-parallel segments. The segments (red areas A' and B') are signatures of the two segments of the subducting slab, the flat one (blue area A) and the steep one (blue area B), respectively. The two segments are independently parallel to the MAT, as typical for subduction zones, while the entire TMVB appears oblique to the MAT if the two segments are considered together. The projected path of the OFZ constitutes the boundary between the two segments. The segmented nature of the TMVB with the off-set in the distance to the trench is a natural explanation for Tzitzio gap in volcanism (Blatter *et al.*, 2007). The sketch of the area is based on Manea *et al.* (2006) and Wilson (1996). Triangles indicate several seismic stations used in the study, circles are the local TMVB volcanoes, OFZ, CFZ, and MAT denote Orozco Fracture Zone, Clipperton Fracture Zone, and Middle America Trench, respectively. The thick grey lines show the boundaries between tectonic plates. Green numbers are the sea floor ages in Ma.

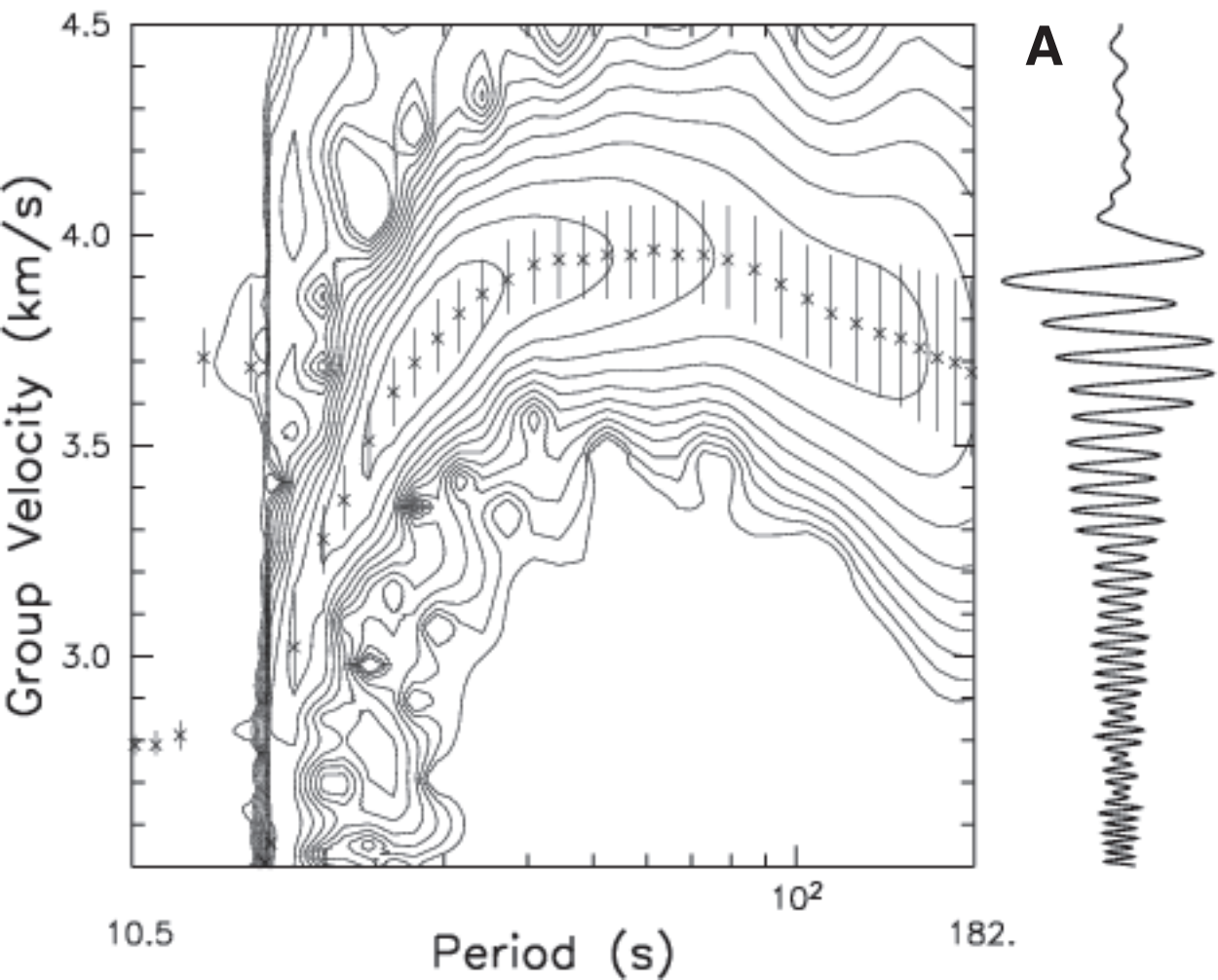




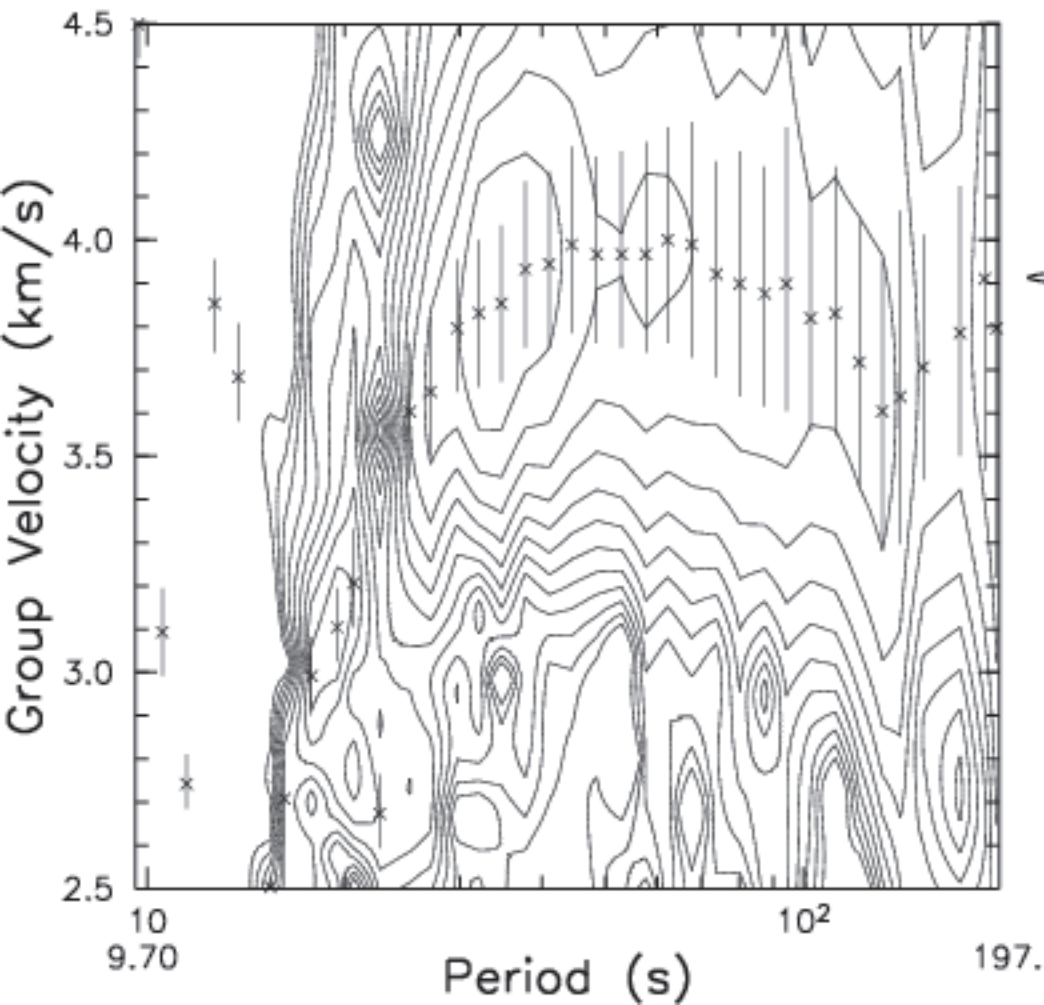




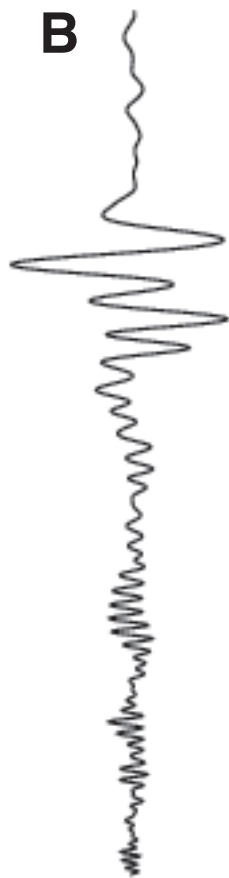
SCIG RAYLEIGH



VENA RAYLEIGH



B



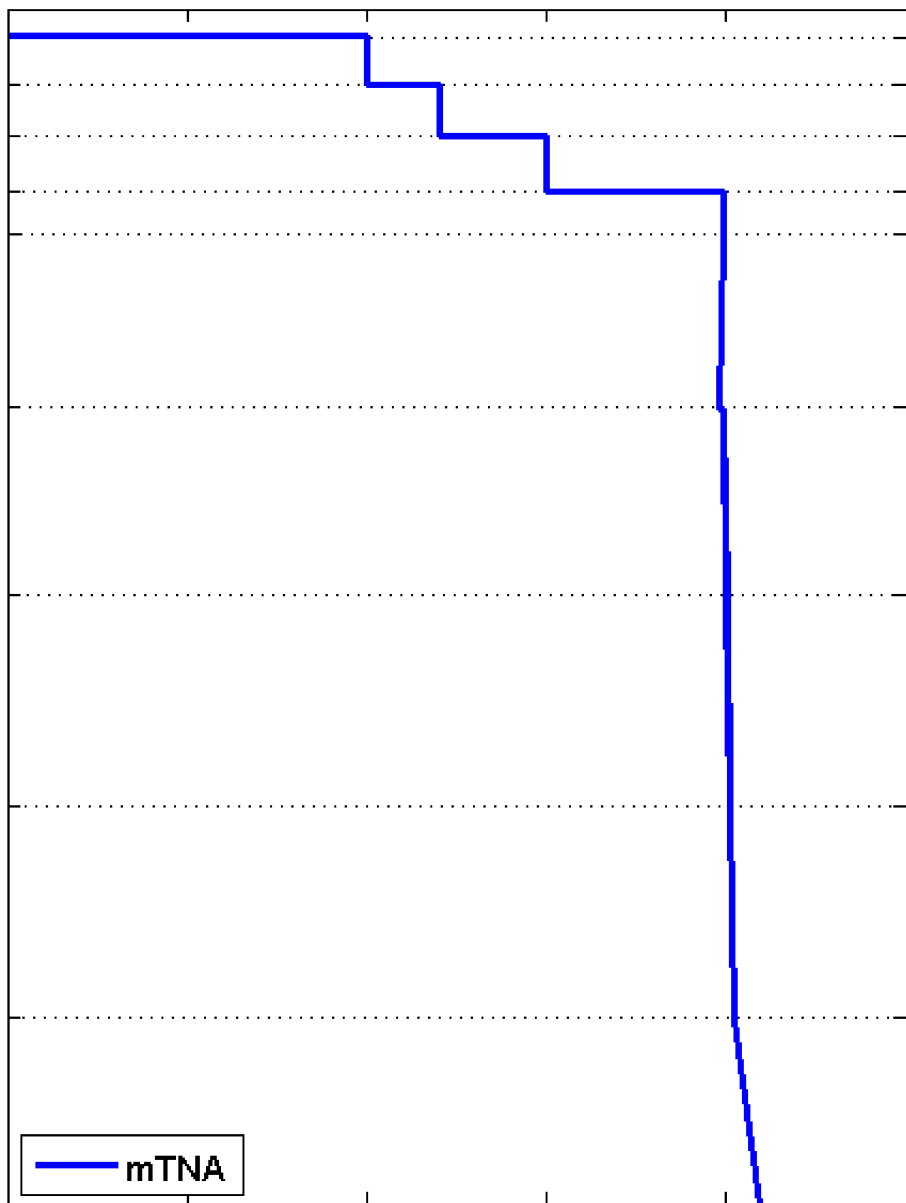
Velocity, km/s

2.5 3 3.5 4 4.5 5

1
11
22
34
43
80
120
165
210

Depth, km

mTNA



depth, km	ρ , kg/m ³	Vp, km/s	Vs, km/s
1.0	2100.0	2.50	1.20
1.0	2700.0	6.00	3.50
11.0	2700.0	6.00	3.50
11.0	2900.0	6.60	3.70
22.0	2900.0	6.60	3.70
22.0	3100.0	7.20	4.00
34.0	3100.0	7.20	4.00
34.0	3580.1	8.04	4.49
43.5	3580.1	8.04	4.49
80.5	3502.0	8.04	4.48
80.5	3502.0	8.04	4.49
120.5	3426.8	8.05	4.50
165.5	3371.1	8.18	4.51
210.5	3324.3	8.30	4.52
210.5	3324.3	8.30	4.52
260.5	3366.3	8.48	4.61
310.5	3411.0	8.66	4.70
360.5	3457.7	8.85	4.78
410.5	3506.8	9.03	4.87
410.5	3931.7	9.36	5.08
460.5	3927.3	9.53	5.19
510.5	3923.3	9.70	5.29
560.5	3921.8	9.86	5.40
610.5	3920.6	10.03	5.50

